



# Understanding intercalation chemistry for sustainable aqueous zinc–manganese dioxide batteries

Yifei Yuan<sup>1,2,6</sup>, Ryan Sharpe<sup>3,6</sup>, Kun He<sup>1,2</sup>✉, Chenghang Li<sup>1</sup>, Mahmoud Tamadoni Saray<sup>2</sup>, Tongchao Liu<sup>4</sup>, Wentao Yao<sup>2</sup>, Meng Cheng<sup>2</sup>, Huile Jin<sup>1</sup>, Shun Wang<sup>1</sup>, Khalil Amine<sup>4</sup>, Reza Shahbazian-Yassar<sup>2</sup>✉, M. Saiful Islam<sup>3,5</sup>✉ and Jun Lu<sup>4</sup>✉

**Rechargeable aqueous Zn–MnO<sub>2</sub> technology combines one of the oldest battery chemistries with favourable sustainability characteristics, including safety, cost and environmental compatibility. However, the ambiguous charge storage mechanism leaves it a challenge to fulfil the great potential of this energy technology. Here we leverage on advanced electron microscopy, electrochemical analysis and theoretical calculations to look into the intercalation chemistry within the cathode material, or  $\alpha$ -MnO<sub>2</sub>, more specifically. We show that Zn<sup>2+</sup> insertion into cathode is unlikely in the aqueous system; rather, the charge storage process is dominated by proton intercalation to form  $\alpha$ -H<sub>2</sub>MnO<sub>2</sub>. We further reveal anisotropic lattice change as a result of entering protons proceeding from the surface into the bulk of  $\alpha$ -MnO<sub>2</sub>, which accounts for the structural failure and capacity decay of the electrode upon cycling. Our work not only advances the fundamental understanding of rechargeable zinc batteries but also suggests the possibility to optimize proton intercalation kinetics for better-performing cell designs.**

**A**queous Zn rechargeable batteries are an emerging sustainable system for grid-scale energy storage due to their low cost, high safety and good performance<sup>1–5</sup>. Various cathode materials have been tried to couple with the Zn anode, among which MnO<sub>2</sub> is particularly attractive owing to its favourable processability, natural abundance and environmental advantages<sup>6–9</sup>. While the application of MnO<sub>2</sub> in alkaline batteries has been plagued by parasitic reactions, recent studies have improved the rechargeability utilizing mild acidic aqueous electrolytes<sup>1,10–12</sup>.

Intensive research efforts have been made to understand the charge storage mechanism of  $\alpha$ -MnO<sub>2</sub>, a common cathode material that adopts a crystal structure with interconnected [MnO<sub>6</sub>] octahedra forming one-dimensional 1×1 and 2×2 tunnels to facilitate reversible ion insertion/extraction<sup>13–16</sup>. However, its working mechanism when coupled with a Zn anode in aqueous mild-acid electrolyte remains under debate. Different mechanisms have been proposed, including (1) Zn<sup>2+</sup> insertion while maintaining the original tunnel configuration<sup>17</sup>; (2) Zn<sup>2+</sup> insertion forming new phases such as spinel ZnMn<sub>2</sub>O<sub>4</sub> (refs. <sup>18,19</sup>) and layered Zn<sub>x</sub>MnO<sub>2</sub> (refs. <sup>20–23</sup>); (3) H<sup>+</sup> insertion forming new phases (MnOOH)<sup>1,24</sup> and (4) H<sup>+</sup>/Zn<sup>2+</sup> co-insertion converting the tunnel host to MnOOH and ZnMn<sub>2</sub>O<sub>4</sub> (refs. <sup>2,25–28</sup>).

While there are reports claiming that the tunnel phase of  $\alpha$ -MnO<sub>2</sub> is transformed completely to a new phase on discharge and recovers subsequently on charge, such high structural reversibility seems to be questionable since previous work points to a high energy demand for charge ordering during tunnel formation<sup>29</sup>. In addition, most bulk-level characterizations detect signals at particle-assembly level and can thus be easily misinterpreted by the presence of side products or electrolyte residuals. It is thus important to elucidate

the charge storage mechanism of this system by examining the precise composition and structure of single MnO<sub>2</sub> particles, preferably down to the atomic level.

To fill this gap, we report combined atomic-level electron microscopy, electrochemistry and theory study of the rechargeable aqueous Zn–MnO<sub>2</sub> battery. Atomic structure imaging shows that the possibility of Zn<sup>2+</sup> intercalation into  $\alpha$ -MnO<sub>2</sub> lattice is extremely low, but reversible H<sup>+</sup> intercalation dominates the process. In addition, the structural inhomogeneity within a single MnO<sub>2</sub> nanowire is revealed, showing that the tunnels on the surface region are distorted seriously with a high degree of anisotropic expansion as a result of H<sup>+</sup> uptake. Ab initio simulations support our experimental observations and provide additional atomic insights, further advancing the fundamental understanding of this battery system.

## Results

**Structure/performance analysis of  $\alpha$ -MnO<sub>2</sub>.** The as-synthesized  $\alpha$ -MnO<sub>2</sub> tunnels are typically occupied by large cations such as K<sup>+</sup> (ref. <sup>30</sup>). We therefore first investigated such cation effects on the performance of MnO<sub>2</sub> cathode by removing K<sup>+</sup> from the tunnels with the results shown in Fig. 1a–c. Before cation removal, the presence of K<sup>+</sup> in tunnel centre can be directly confirmed by energy-dispersive X-ray spectroscopy (EDS) and atomic imaging (Fig. 1d). After K<sup>+</sup> removal, Fig. 1a–c shows no sign of K<sup>+</sup>, leaving the tunnel space essentially empty and its framework well maintained. Note that  $\alpha$ -MnO<sub>2</sub> exhibits a nanowire-like morphology (Fig. 1a) with [001] axial direction (also the tunnel direction). Figure 1b shows the [001]-projection of ultramicrotomed  $\alpha$ -MnO<sub>2</sub> nanowire (its axial direction) while Fig. 1c shows the [010]-projection

<sup>1</sup>College of Chemistry and Materials Engineering, Wenzhou University, Wenzhou, China. <sup>2</sup>Mechanical and Industrial Engineering, University of Illinois at Chicago, Chicago, IL, USA. <sup>3</sup>Department of Chemistry, University of Bath, Bath, UK. <sup>4</sup>Chemical Sciences and Engineering Division, Argonne National Laboratory, Lemont, IL, USA. <sup>5</sup>Department of Materials, University of Oxford, Oxford, UK. <sup>6</sup>These authors contributed equally: Yifei Yuan, Ryan Sharpe. ✉e-mail: [hekun@wzu.edu.cn](mailto:hekun@wzu.edu.cn); [rsyassar@uic.edu](mailto:rsyassar@uic.edu); [saiful.islam@materials.ox.ac.uk](mailto:saiful.islam@materials.ox.ac.uk); [junlu@anl.gov](mailto:junlu@anl.gov)

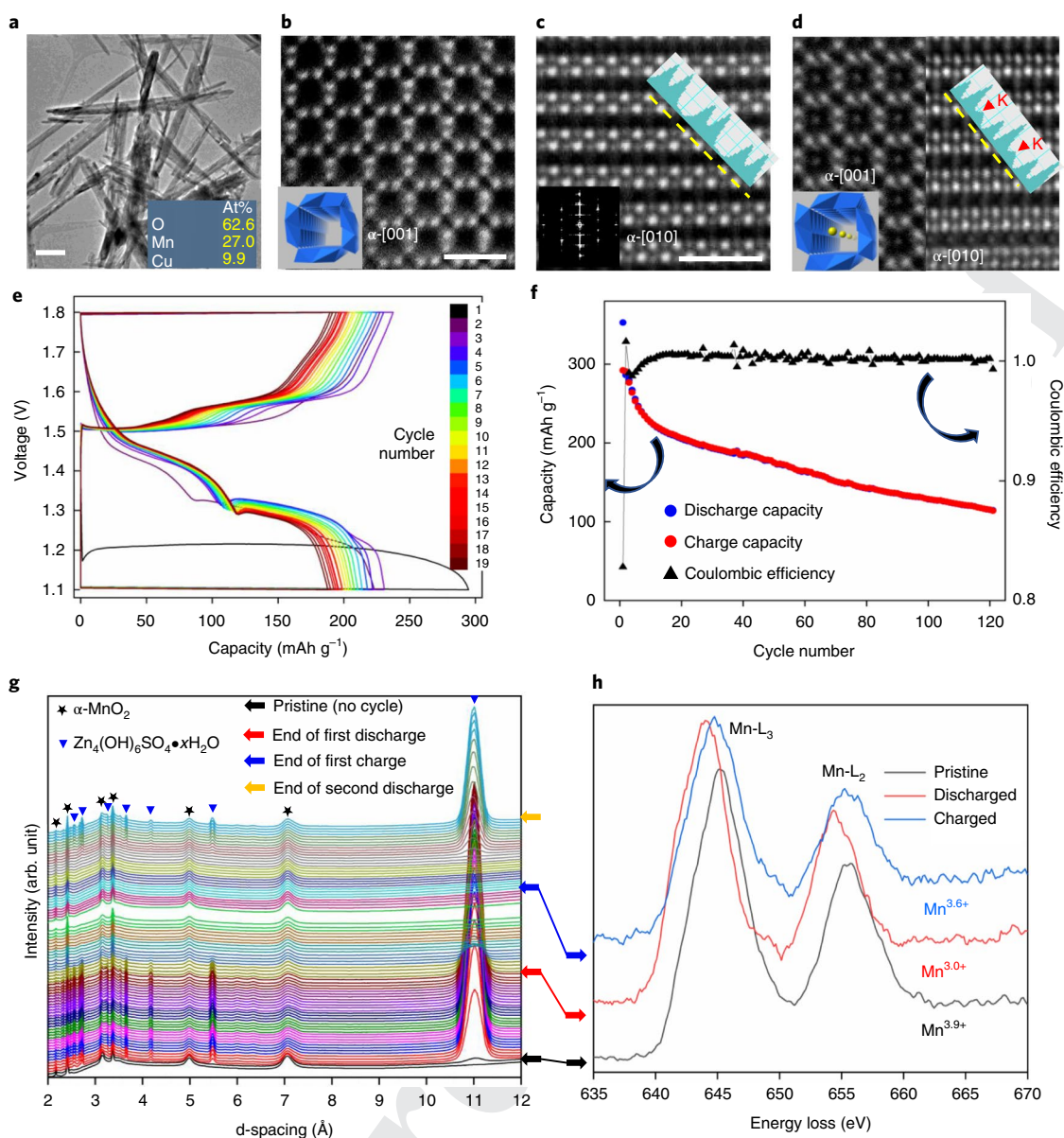


**Fig. 1 | Structure analysis and battery performance of  $\alpha$ -MnO<sub>2</sub>.** **a**, Low-magnification TEM image showing the morphology of  $\alpha$ -MnO<sub>2</sub> nanowires without K<sup>+</sup>. Insets are EDS quantification. **b**, [001] down-tunnel imaging (along nanowire axis) showing the atomic structure of  $\alpha$ -MnO<sub>2</sub> without K<sup>+</sup> occupying the tunnel. Each bright dot in the image represents an Mn atomic column. Insets are the corresponding polyhedral model. **c**, [010] zone axis (nanowire radial direction) imaging showing the atomic structure of  $\alpha$ -MnO<sub>2</sub> tunnels without K<sup>+</sup>. Inset profiles the intensity distribution over the yellow dashed line. **d**, [001] and [010] axes imaging showing the atomic structure of  $\alpha$ -MnO<sub>2</sub> nanowires with K<sup>+</sup> occupying the tunnel centre position. The red arrows in the line profile indicate presence of K<sup>+</sup>. Inset is the corresponding polyhedral model with K<sup>+</sup> (yellow dots) at Wyckoff 2a sites. Scale bars in **a** and **b-d** are 100 nm and 1 nm, respectively. **e**, Voltage profiles of the first 19 cycles of a Zn–MnO<sub>2</sub> battery. **f**, The specific discharge/charge capacity (left y axis) and the Coulombic efficiency (right y axis) on cycling. **g**, In situ XRD showing the structural evolution of  $\alpha$ -MnO<sub>2</sub> electrode during the first cycle and the second discharge. **h**, EELS analysing Mn valence for the pristine, discharged and charged samples.

(its radial direction). More crystallographic/imaging details are given in Supplementary Fig. 1 (Supplementary Note 1).

The voltage profiles of the aqueous Zn–MnO<sub>2</sub> batteries with and without K<sup>+</sup> are given in Supplementary Fig. 2. Both profiles exhibit a single plateau between 1.2 and 1.3 V for the first discharge reaction and two plateaus at 1.5 V and 1.6 V for the first charge. For the subsequent cycles, the two-plateau phenomenon is reproducible for both charge (1.5 V and 1.6 V) and discharge (1.45 V and 1.3 V). The high consistency of the voltage profiles for  $\alpha$ -MnO<sub>2</sub> with and without K<sup>+</sup> points to a similar charge storage mechanism in both cases. The K<sup>+</sup> within the tunnels is relatively stable upon cycling as further

confirmed in Supplementary Fig. 3, implying a weak charge carrier K<sup>+</sup> interaction.

Our aim to test the possibility of Zn<sup>2+</sup> intercalation into the tunnel may have been compromised by the presence of K<sup>+</sup> in the tunnels; we therefore focus on the case of K<sup>+</sup>-free  $\alpha$ -MnO<sub>2</sub> in the following discussion considering their electrochemical similarities discussed in the preceding. The voltage profiles of an aqueous Zn–MnO<sub>2</sub> (K<sup>+</sup>-free) battery are depicted in Fig. 1e. It is noticeable that with the increase of cycling number, the discharge capacity contributed from the first plateau (~1.45 V) changes in a different way from that of the second plateau (1.3 V). The first-plateau capacity keeps

increasing with cycling, while the second-plateau capacity decreases more obviously, resulting in an overall decreasing discharge capacity with cycling. This phenomenon implies that the charge storage mechanisms for these two discharge plateaus are different. We also measured the cycling performance (Fig. 1f), showing that the first discharge capacity is above  $300 \text{ mAh g}^{-1}$ , close to the theoretical capacity assuming all Mn reduced to  $\text{Mn}^{2+}$  on charge carrier insertion. However, on cycling, both discharge and charge capacity clearly decrease. After 120 cycles, the capacity drops to  $\sim 100 \text{ mAh g}^{-1}$ . By contrast, the Coulombic efficiency is roughly maintained at 100%, except for the first few cycles. This indicates that the capacity drop with cycling is caused by the irreversible structural change of the electrode material itself, which we return to later. Decent long-term cycling performance of Zn– $\text{MnO}_2$  batteries at high rates has been reported previously<sup>1,2,20,22</sup>. Several key factors could contribute to the reported high performance but are not implemented in our work, for example, the use of  $\text{Mn}^{2+}$  additives in the electrolyte, the phase/morphology control and surface engineering of  $\text{MnO}_2$ . In our work, with a main focus on fundamental understanding, these performance-enhancing strategies are not applied so as to highlight the electrode's working mechanisms.

To further study the phase evolution during cycling, in situ X-ray diffraction (XRD) was used (Fig. 1g). It shows that the characteristic peaks of  $\alpha\text{-MnO}_2$  remain noticeable throughout the whole discharge–charge process, indicating that the tunnel phase is preserved. However, these peaks exhibit slight broadening towards the larger d-spacing direction during discharge, possibly due to a strain or distortion effect. New peaks immediately appear at d-spacings of 1.1 nm, 0.55 nm and 0.42 nm at the beginning of discharge, and their intensity increases during discharge and decreases during charge. This phenomenon points to reversible phase transition upon cycling, which should be different from the  $\text{MnO}_2$ -related structural evolution and will be later analysed in the discussions of Fig. 2. Notably, these results fail to explain the difference in mechanism between the first and second voltage plateaus within one discharge reaction, implying the significance of underlying kinetic factors. To track the Mn valence change, electron energy-loss spectroscopy (EELS) is applied (Fig. 1h). According to the literature<sup>31</sup> and our quantification analyses, the Mn valence is seen to decrease from 3.9+ to 3.0+ during discharge and increase back to 3.6+ (rounded values) when charged, implying that the change of Mn valence is largely reversible upon cycling. Refer to Supplementary Fig. 4 and Supplementary Note 1 for details.

**Microscopy analysis of  $\text{H}^+$  versus  $\text{Zn}^{2+}$  insertion.** The preceding discussions indicate the existence of a reversible Faradaic charge storage reaction in single  $\alpha\text{-MnO}_2$  particles. Intensive focus is thus put into the microscopic exploration of discharged  $\alpha\text{-MnO}_2$  structure. Figure 2a–d shows the scanning transmission electron microscopy–(STEM–) EDS analysis for a single  $\text{MnO}_2$  nanowire after the first discharge process. The nanowire largely maintains its shape with its surface unevenly covered by flake-like pieces (Fig. 2a). The EDS mapping (Fig. 2b) shows that while the distribution of Mn and O reflects the shape of  $\text{MnO}_2$  nanowire, Zn stays within the flake-like pieces, not within the  $\text{MnO}_2$  nanowire, indicating a low possibility of  $\text{Zn}^{2+}$  insertion into  $\text{MnO}_2$  lattice. Furthermore, the nanowire is seen to be composed mainly of Mn and O ( $\text{MnO}_2$ ) without Zn presence (Fig. 2a insets). More statistical STEM–EDS analyses are provided in Supplementary Fig. 5 to demonstrate that  $\text{Zn}^{2+}$  did not insert into the  $\text{MnO}_2$  lattice. Instead, with an aqueous  $\text{ZnSO}_4$  electrolyte (mild acidic,  $\text{pH} \sim 4.8$ ), we suggest that the dominant charge storage mechanism is intercalation of  $\text{H}^+$  ions into the  $\text{MnO}_2$  tunnels without noticeable phase transition.

The hypothesis of a proton intercalation mechanism is further tested by EDS analysis of the flake-like pieces generated during discharge (Fig. 2a, inset), which are rich in Zn, O and S, with a Zn/S

atomic ratio of  $\sim 4$ . Combined with the in situ XRD results in Fig. 1g revealing emerging peaks at  $\sim 1.1 \text{ nm}$ , one can reasonably claim these pieces to be  $\text{Zn}_4(\text{OH})_6\text{SO}_4 \cdot x\text{H}_2\text{O}$  possessing a large layer spacing of  $\sim 1.1 \text{ nm}$  supported by water molecules. The fact that this phase contains a large amount of  $\text{OH}^-$  points to an  $\text{OH}^-$ -rich electrolyte as a result of  $\text{H}^+$  insertion into the tunnels. Both the in situ XRD (Fig. 1g) and the ex situ transmission electron microscopy (TEM) analyses (Supplementary Fig. 6) confirm that  $\text{Zn}_4(\text{OH})_6\text{SO}_4 \cdot x\text{H}_2\text{O}$  can be reversibly formed/decomposed during discharge/charge. The lattice positions of the inserted protons as  $\text{OH}^-$  groups within the  $\alpha\text{-MnO}_2$  tunnels are addressed by ab initio modelling discussed in the following. It is worth mentioning that the previous studies proposing  $\text{Zn}^{2+}$  insertion into  $\text{MnO}_2$  generally relied on (EDS) elemental analysis of the discharged  $\text{MnO}_2$  electrode<sup>2,23</sup>, whose accuracy could be compromised as it might not be able to distinguish the Zn signals from the residual salts or other by-products (for example,  $\text{Zn}_4(\text{OH})_6\text{SO}_4 \cdot x\text{H}_2\text{O}$  revealed in this work) adjacent or attached to  $\text{MnO}_2$  particles. Additional evidence excluding  $\text{Zn}^{2+}$  insertion is provided by discussing the performance of an aprotic Zn– $\text{MnO}_2$  battery (Supplementary Fig. 7).

Another key evidence excluding the possibility of  $\text{Zn}^{2+}$  insertion is the direct atomic imaging of discharged  $\text{MnO}_2$  along its various zone axes (Fig. 2c–d). The radially projected imaging (Fig. 2c) shows that the tunnels are essentially empty without the presence of  $\text{Zn}^{2+}$  as their occupation in the tunnels would have resulted in a brighter contrast in the line profile (Fig. 2c inset); indeed, the actual profile shows only the presence of Mn atomic columns. The tunnel structure is maintained after discharge as indicated by the fast Fourier transform showing a typical  $\alpha\text{-MnO}_2$ -[010] pattern. Imaging down the tunnels in Fig. 2d directly confirms that  $\alpha\text{-MnO}_2$  tunnels are well maintained and unoccupied by any heavy cations ( $\text{Zn}^{2+}$  or  $\text{K}^+$ ), indicating that  $\text{H}^+$  insertion should be the dominant mechanism. Note that the previous study<sup>1</sup> reported a seemingly similar mechanism of  $\text{H}^+$  insertion in  $\alpha\text{-MnO}_2$ , in which the discharge product of  $\text{MnO}_2$  nanofibres was found to be much shorter  $\text{MnOOH}$  nanorods with different morphology and phase (denoted as  $\alpha\text{-MnO}_2 + \text{H}^+ + \text{e}^- = \text{MnOOH}$ ). By contrast, our findings point to a completely different mechanism featuring  $\text{H}^+$  intercalation into  $\text{MnO}_2$  with the original tunnel phase and nanowire morphology largely maintained (denoted as  $\alpha\text{-MnO}_2 + \text{H}^+ + \text{e}^- = \alpha\text{-H}_1\text{MnO}_2$ ).

Figure 2e–h depicts the atomic analysis of discharged  $\text{MnO}_2$  along its tunnel direction. Interestingly, the tunnel structures, although well maintained after discharge, exhibit non-uniform lattice distortion, particularly when comparing the tunnels close to the surface region with those in the bulk (Fig. 2e). Within the bulk,  $\text{MnO}_2$  maintains its tetragonal symmetry without major distortion; by contrast, close to the surface region, lattice distortion is obvious with the tunnels severely distorted. Moreover, the distortion appears in an ordered fashion; that is, the tunnels close to the surface are all distorted along one specific direction. This results in the increase of lattice parameter  $a$  and decrease of lattice parameter  $b$ , causing the deviation from the initial tetragonal symmetry ( $a$ – $b$  angle ( $\gamma$ ) reduced to  $85^\circ$ ) as illustrated in Fig. 2e,h (and supported by atomistic modelling detailed in the following). Such a symmetry change is less obvious within the bulk region ( $a$ – $b$  angle ( $\gamma$ ) close to  $90^\circ$ ) although there is a similar  $a$ -increase and  $b$ -decrease trend.

There are a few studies reporting the direct microscopic imaging of hydrogen atoms in well-crystallized hydrides such as  $\text{YH}_2$  and  $\text{TiH}$  (refs. <sup>32,33</sup>); achieving this goal in  $\text{MnO}_2$  is, however, quite challenging for several reasons. First,  $\text{H}^+$  are electrochemically inserted into  $\text{MnO}_2$  as ‘foreign or dopant species’, distorting the host lattice and thus disturbing direct  $\text{H}^+$  imaging. Second,  $\text{H}^+$  imaging requires a sufficiently thin sample, for example, 8 nm for H imaging in  $\text{YH}_2$  (ref. <sup>32</sup>); however, it is technically challenging to achieve so in our work. Third, electrochemically inserted  $\text{H}^+$  coordinated to oxygen has an O–H bond length of 0.10 nm as discussed in the next

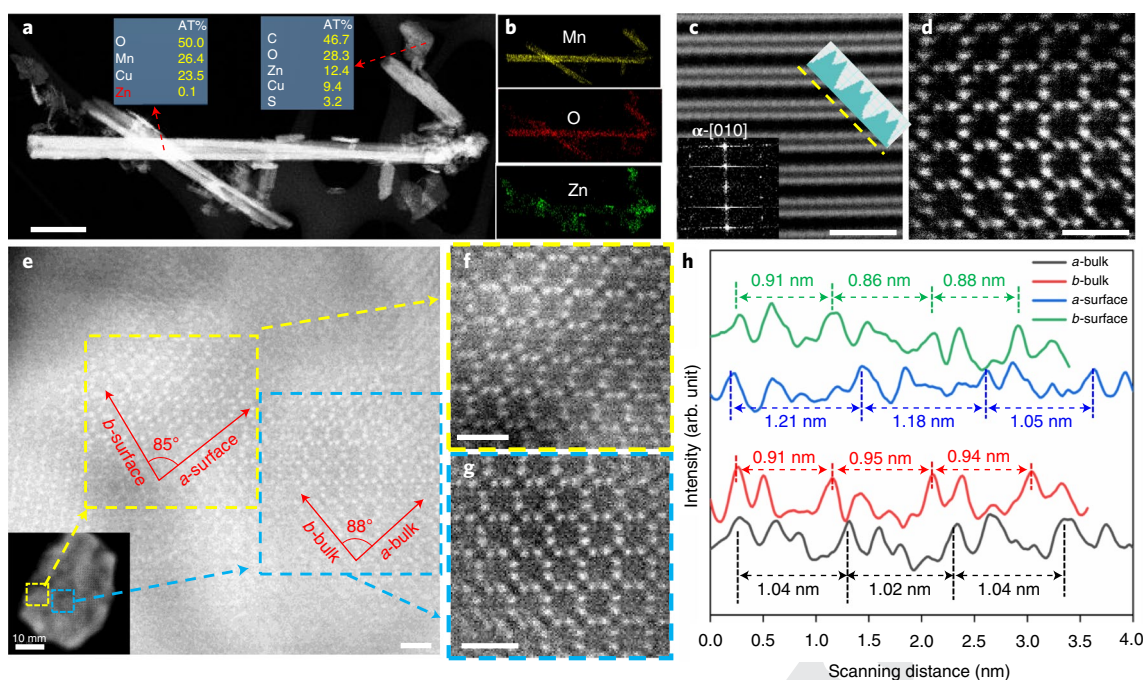


**Fig. 2 | STEM analysis of discharged  $\alpha$ -MnO<sub>2</sub> nanowires.** **a–d**, High-angle annular dark field (HAADF)/EDS analyses showing the nanowire with flake-like pieces adhered to its surface (insets are site-specific compositional quantification) (**a**), STEM-EDS elemental mapping of Zn, Mn and O (**b**) and the atomic scale [010] (**c**) and [001] projections (**d**) of MnO<sub>2</sub> demonstrating essentially ‘empty’ tunnels without presence of heavy cations. **e–h**, Down-tunnel imaging (**e–g**) and line profiles (**h**) depicting the non-uniform and anisotropic tunnel distortion resulted from H<sup>+</sup> intercalation, where **f** and **g** are the atomic-scale imaging from the surface (**f**) and the bulk (**g**) regions, and the line profiles are drawn exactly along the red arrows (also the *a*–*b* vector directions) indicated in **e**. Scale bars in **a** and **c–g** are 100 nm and 1 nm, respectively.

section, which is quite close to the resolution limit of the microscope (0.08 nm).

Note that the microscopic structural features revealed in the preceding could not be caused by electron beam effect/damage, which is addressed in Supplementary Note 1. Moreover, the coordinated anisotropic lattice distortion of discharged MnO<sub>2</sub> implies that H<sup>+</sup> intercalation follows an energetically favourable pathway, necessitating the implementation of ab initio modelling.

**Atomistic modelling of H<sup>+</sup> versus Zn<sup>2+</sup> insertion.** There are limited studies attempting to characterize the local structural positions or perturbations resulting from proton insertion in  $\alpha$ -MnO<sub>2</sub>, due largely to the difficulty in probing the exact positions of such tiny ions. To complement our microscopy work, we use ab initio simulations based on density functional theory (DFT) to examine the effect of H<sup>+</sup> and Zn<sup>2+</sup> insertion and to identify the preferred proton (OH) positions in  $\alpha$ -H<sub>x</sub>MnO<sub>2</sub> ( $0 \leq x \leq 1$ ), extending our previous computational work on MnO<sub>2</sub> (refs. <sup>34,35</sup>). (The computational methods are detailed in Methods and Supplementary Note 2). Previous DFT studies<sup>36,37</sup> have examined H<sup>+</sup> insertion in other polymorphs of MnO<sub>2</sub> ( $\gamma$ - and  $\beta$ -MnO<sub>2</sub>) but have not focused on both Zn<sup>2+</sup> and H<sup>+</sup> insertion in the Zn/ $\alpha$ -MnO<sub>2</sub> system.

We first investigate the possible sites for proton insertion into the large 2 × 2 and small 1 × 1 tunnels of  $\alpha$ -H<sub>x</sub>MnO<sub>2</sub> by examining numerous configurations and their energetics at each composition (*x*). The lowest energy structures of  $\alpha$ -H<sub>x</sub>MnO<sub>2</sub> (*x* = 0.25, 0.5, 0.75 and 1.0) are illustrated in Fig. 3a–d, which shows the positions and orientations of the OH groups formed by the inserted protons bonding to lattice oxygen ions. Two main features emerge. First, for  $0 < x \leq 0.5$ , our results indicate that insertion adjacent to the trigonal pyramidal oxygen in the 2 × 2 tunnel has the lowest energy (Fig. 3a); the O–H bond length has a typical value of 0.10 nm. As expected, the calculations indicate that Mn is reduced from 4+ to 3+ as H<sup>+</sup> is

inserted. Second, for  $x > 0.5$ , we find that insertion into the smaller 1 × 1 tunnel in addition to the 2 × 2 tunnel becomes favourable (Fig. 3c). The resulting structures indicate that the H<sup>+</sup> ions distribute as uniformly as possible to minimize the ion–ion electrostatic repulsion; for example, this feature is illustrated by the low energy structure of  $\alpha$ -H<sub>0.5</sub>MnO<sub>2</sub> containing two H<sup>+</sup> ions in each adjacent 2 × 2 tunnel (Fig. 3b). This result also accords with our previous DFT studies investigating Li<sup>+</sup>/Na<sup>+</sup> insertion in  $\alpha$ -MnO<sub>2</sub> (ref. <sup>38</sup>).

The high levels of proton insertion are also important to structural changes. The variations in the calculated lattice parameters and unit cell volume of  $\alpha$ -H<sub>x</sub>MnO<sub>2</sub> as a function of *x* are plotted in Fig. 3e. The unit cell volume expands with increasing *x*, which is attributed partly to the increase of the effective ionic radii of Mn on reduction from Mn<sup>4+</sup> (0.53 Å) to Mn<sup>3+</sup> (0.645 Å). The change in unit cell volume of protonated H<sub>x</sub>MnO<sub>2</sub> structures exhibit a nonlinear dependence, expanding by only +4% up to *x* = 0.5 but by +16% at *x* = 1.0. This significant structural change from *x* = 0.5 and the aforementioned change of proton positions from 2 × 2 tunnels to 1 × 1 tunnels may be related to the two-plateau feature of the voltage profiles (Fig. 1e). It can then be reasonably proposed that the elongation of the first discharge plateau (~1.45 V) and the shortening of the second discharge plateau (1.3 V) upon cycling could be directly related to the change of H<sup>+</sup> insertion kinetics in 2 × 2 tunnels (for the first plateau) and 1 × 1 tunnels (for the second plateau), respectively. To test this hypothesis, the diffusion coefficient of H<sup>+</sup> as a function of discharge capacity and the cyclability of two MnO<sub>2</sub> electrodes when discharged to 1.1 V versus 1.32 V are measured and discussed (Supplementary Figs. 9 and 10); the results indicate that the second plateau exhibits much poorer H<sup>+</sup> insertion kinetics.

Regarding the crystal structure, the ab initio simulations also show that the lattice symmetry changes with the *a*–*b* angle ( $\gamma$ ), decreasing from 90.0° to 88.5° on proton insertion to form HMnO<sub>2</sub>, in good agreement with our experiments (~88° in bulk HMnO<sub>2</sub>;

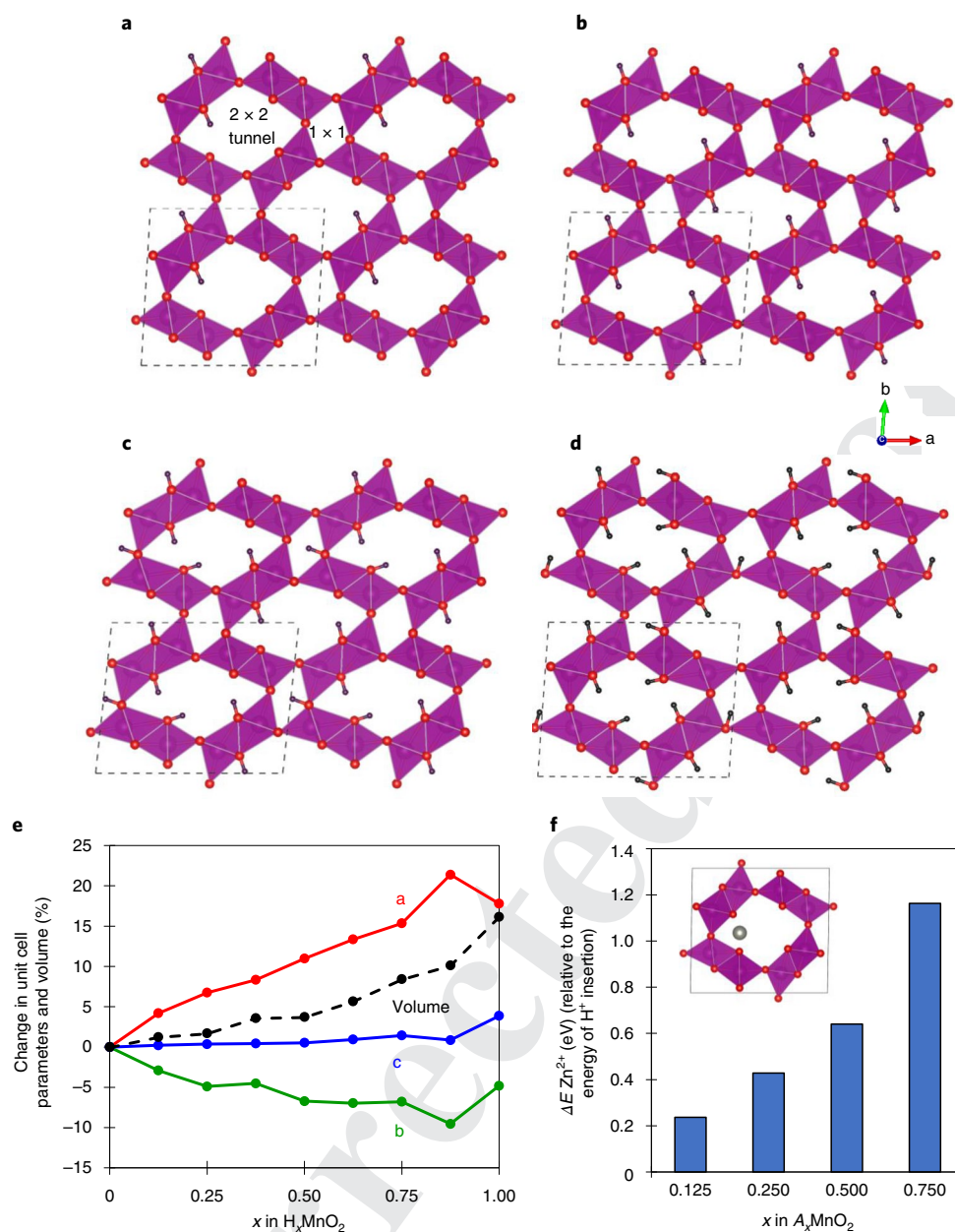


**Fig. 3 | Atomistic modelling of  $H^+$  (versus  $Zn^{2+}$ ) insertion. a–d.** Lowest energy structures obtained for  $\alpha$ - $H_xMnO_2$  when  $x=0.25$  (a),  $x=0.5$  (b),  $x=0.75$  (c) and  $x=1.0$  (d). Mn, O and H are shown by purple, red and black, respectively. Representative unit cells are highlighted by dashed lines; for example, for  $H_{0.25}MnO_2$ , one H ion is in the central  $2 \times 2$  tunnel and one H ion is in the top left  $2 \times 2$  tunnel to give  $H_2Mn_8O_{16}$  in total, or the stoichiometry  $H_{0.25}MnO_2$ . Structures for additional compositions  $x=0.125, 0.375, 0.625$  and  $0.875$  are provided in Supplementary Fig. 8. **e.** Calculated percentage changes in the unit cell parameters ( $a$ ,  $b$  and  $c$ ) and volume as  $H^+$  is inserted into  $H_xMnO_2$  ( $0 < x \leq 1$ ). **f.** Change in the energy of  $Zn^{2+}$  insertion relative to the energy of  $H^+$  insertion into  $A_xMnO_2$ , where  $x$  is 0.125, 0.25, 0.5 and 0.75 and  $A$  is  $H^+$  or  $Zn^{2+}$  (listed in Supplementary Table 3). Insertion energies for H and Zn into  $MnO_2$  were calculated by comparing the energy of empty  $MnO_2$  and an  $H_2$  molecule or Zn metal with the atom intercalated within  $A_xMnO_2$  ( $A=H$  or  $Zn$ ) as a function of  $x$ . Inset shows, as an example, the calculated lowest energy structure of  $Zn_{0.125}MnO_2$ .

Fig. 2e). This result is highlighted in Fig. 3e, showing the calculated increase of up to 20% in lattice parameter  $a$  and the decrease of up to 10% in  $b$ , also observed experimentally (Fig. 2h). Hence, our atomistic simulations have helped to quantify the anisotropic tunnel structural change along the  $a$  and  $b$  directions and the consequent symmetry change. From experiment, the lattice distortion is more obvious in the particle surface region probably due to the diffusion-controlled  $H^+$  insertion kinetics. The DFT results also confirm that, despite the tunnel expansion and symmetry change, the tunnels themselves remain intact and do not collapse

on proton intercalation. We note that ab initio molecular dynamics simulations of protonated  $\alpha$ - $MnO_2$  (Supplementary Note 2 and Supplementary Fig. 11) indicate no long-range proton conduction via hopping between oxygen sites.

We used DFT methods to further investigate whether  $H^+$  or  $Zn^{2+}$  insertion into  $MnO_2$  is preferred. The approach used to identify the possible  $Zn^{2+}$  insertion sites is discussed in Supplementary Note 3 and Supplementary Fig. 12 and follows our previous studies investigating  $Li^+/Na^+$  insertion into  $\alpha$ - $MnO_2$  (ref. 38). Figure 3f shows the energy of  $Zn^{2+}$  insertion into  $Zn_xMnO_2$  as a function of Zn content

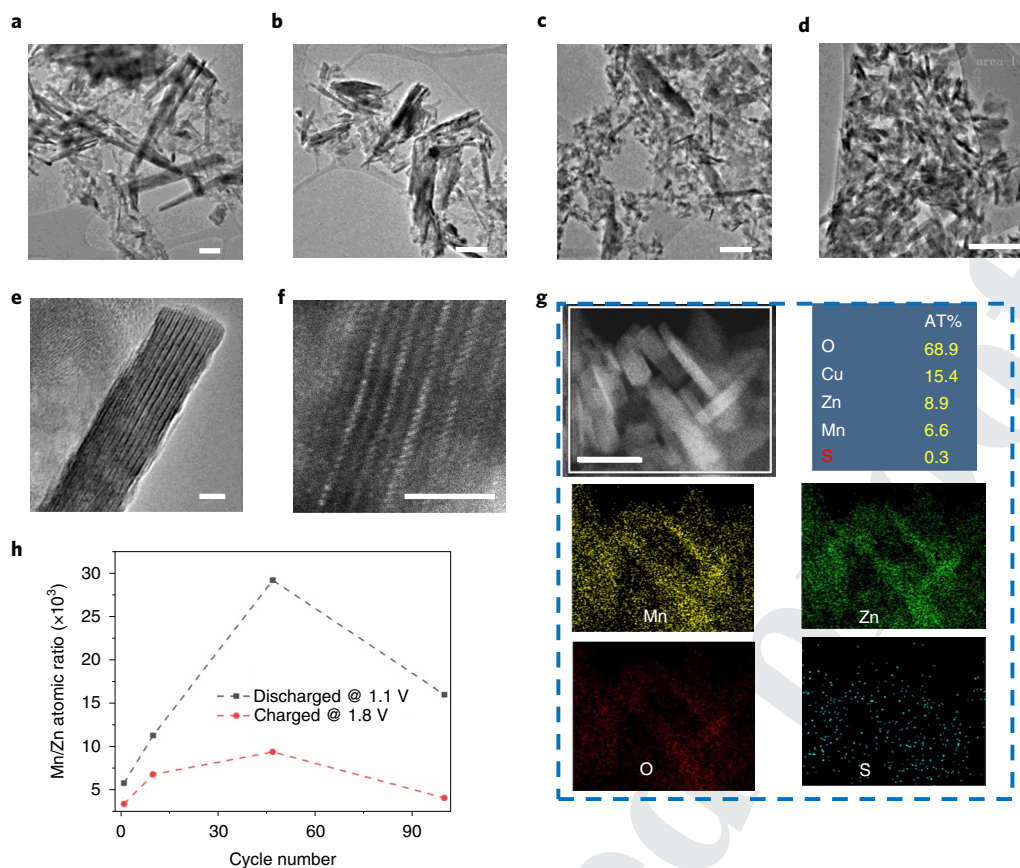


**Fig. 4 | Morphological/structural analysis of the  $\alpha$ - $\text{MnO}_2$  electrode during long cycling conditions.** **a–d**, Low-magnification TEM images of the scratched sample from the  $\text{MnO}_2$  electrode with 1 cycle (**a**), 10 cycles (**b**), 50 cycles (**c**) and 100 cycles (**d**). **e, f**, High-resolution TEM (**e**) and atomic STEM-HAADF (**f**) images showing the layered structure of the tiny nanograins formed after cycles. **g**, STEM-EDS analysis showing the compositional quantification of the tiny nanograins as well as the elemental distribution. **h**, ICP-evaluated Mn/Zn atomic ratio in the electrolyte as a function of cycling number, where both discharged and charged electrolytes are analysed. Scale bars in **a–d** are 100 nm, in **e, f** they are 3 nm and in **g** they are 50 nm.

(x), relative to the corresponding  $\text{H}^+$  insertion energy. An important finding is that at low content ( $x=0.125$ ),  $\text{Zn}^{2+}$  insertion is already unfavourable compared with proton insertion. As  $x$  increases,  $\text{Zn}^{2+}$  insertion becomes increasingly energetically unfavourable. This result is in agreement with our STEM analysis and other experimental studies<sup>1,24</sup> in which there is no evidence for  $\text{Zn}^{2+}$  insertion.

As discussed in the Introduction, previous studies also proposed a charge storage mechanism of co-insertion of  $\text{H}^+$  and  $\text{Zn}^{2+}$  into  $\text{MnO}_2$  lattice<sup>2,25,26</sup>. To probe the possibility that the two-step discharge plateau (Fig. 1e) is caused by the insertion of  $\text{H}^+$  and then  $\text{Zn}^{2+}$ , we investigated  $\text{Zn}^{2+}$  insertion into  $\alpha$ - $\text{H}_{0.5}\text{MnO}_2$  using DFT. The most stable  $\text{Zn}^{2+}$  insertion site was in the  $1 \times 1$  tunnel (Supplementary Fig. 12), but this configuration was still found to be higher in energy (221 meV per formula unit) than inserting another proton into  $\alpha$ - $\text{H}_{0.5}\text{MnO}_2$ . This indicates that, even after initial proton intercalation up to  $\text{H}_{0.5}\text{MnO}_2$ ,  $\text{Zn}^{2+}$  insertion remains unfavourable. In short, our combined experimental and computational results indicate that  $\text{H}^+$  insertion is always more favourable than either  $\text{Zn}^{2+}$  insertion or  $\text{Zn}^{2+}/\text{H}^+$  co-insertion.

**Mechanism for cycling-induced capacity decay.** As  $\text{H}^+$  intercalation/extraction continues for several cycles, the  $\text{MnO}_2$  host will experience repetitive Mn valence change together with lattice distortion/recovery. A possible hypothesis is that the capacity decay of the  $\text{MnO}_2$  cathode on cycling could be caused by loss of active  $\text{MnO}_2$  mass, which is testified in Supplementary Fig. 13. Figure 4 further explores the structural change of the electrode during

cycling. One can tell that  $\text{MnO}_2$  nanowires gradually decompose on cycling; after 100 cycles, the nanowire-like particles can hardly be seen. In addition, after 50 cycles, some tiny needle-like nanograins appear, whose diameter and length seem to be independent of cycle number while their number keeps increasing, making them a major component after 100 cycles (Fig. 4c,d). See Supplementary Fig. 14 for more evidence and discussion. TEM analyses in Fig. 4e,f demonstrate that these cycling-induced nanograins have a large interlayer spacing of  $\sim 1$  nm and that within two adjacent layers lies another layer featuring lower-contrast atoms. These tiny nanograins are rich in Zn, Mn and O but poor in S, exhibiting a Zn/Mn ratio of  $\sim 3/2$  (Fig. 4g). See Supplementary Fig. 15 for more statistical analyses. The Zn-rich nature of these nanograins indicates that there cannot be any  $\text{Zn}^{2+}$ -inserted manganese oxides derived from the  $\text{MnO}_2$  host; rather, they are some precipitated phases from the electrolyte when it is rich in  $\text{Zn}^{2+}$  and  $\text{Mn}^{2+}$  as a result of  $\text{Mn}^{2+}$  dissolution during the discharge process. See Supplementary Figs. 4c, 16 and 17 for more analyses of such tiny nanograins. It is worth mentioning that these cycling-induced nanograins seem to be irreversible. Once they are formed and attached to the electrode, they cannot be electrochemically decomposed during the charge process (Supplementary Fig. 16), which could account for the capacity decay of  $\text{MnO}_2$  cathode.

To test the mechanism of  $\text{Mn}^{2+}$  dissolution and irreversible Zn–Mn–O nanograin precipitation for capacity decay, inductively coupled plasma (ICP) analysis of the electrolytes with different cycles is carried out. The Mn concentration in the electrolyte is evaluated

with reference to the Zn concentration, with the latter considered to be relatively constant. The Mn/Zn ratios in the electrolyte solutions collected after different cycles are shown in Fig. 4h. One can tell that within 50 cycles, the Mn concentration keeps increasing, indicating the gradual accumulation of dissolvable  $\text{Mn}^{2+}$  in the electrolyte as a result of  $\text{H}^+$  intercalation and  $\text{Mn}^{3+}$  disproportionation reaction. For the charged electrolyte, the  $\text{Mn}^{2+}$  concentration largely decreases but also exhibits a slight increasing trend with cycle number; this indicates that the  $\text{Mn}^{3+}$  disproportionation reaction is largely but not totally reversible and that  $\text{MnO}_2$  gradually loses its active mass on cycling. After 50 cycles, however, for both the discharged and charged electrolytes, the Mn concentration decreases with increasing cycle number, which points to the reprecipitation of  $\text{Mn}^{2+}$  with the irreversible formation of tiny nanograins as discussed.

## Discussion

Compared with energy storage technologies based on lithium ions, rechargeable aqueous Zn batteries are much closer to entering the stationary battery market owing to their low cost, high safety and environmental friendliness, which form the important dimensions of sustainability. Yet it is exactly the use of aqueous electrolyte that complicates the essential electrochemistry and introduces mechanistic ambiguity, which consequently compromises the sustainability of aqueous batteries. In this respect, this work provides atomic insights into the mechanisms of the representative aqueous Zn– $\text{MnO}_2$  battery and points to future strategies for sustainability enhancement, such as the tuning of proton insertion kinetics and the suppression of Mn dissolution. Furthermore, the unveiled critical role of proton insertion could inspire the development of more sustainable systems beyond Zn– $\text{MnO}_2$  battery where aqueous electrolyte is present with the potentially important role of proton insertion.

## Methods

**Material synthesis.** The  $\alpha$ - $\text{MnO}_2$  nanowires are prepared by a hydrothermal reaction.  $\text{KMnO}_4$  (0.9878 g) and  $\text{MnSO}_4 \cdot \text{H}_2\text{O}$  (0.4226 g) are mixed in 80 ml deionized (DI) water to form a purple solution. The obtained slurry was then sealed into a 100 ml autoclave and heated at 160 °C for 12 h. After centrifugation and DI water wash of the obtained products, a four-day acid treatment using concentrated  $\text{HNO}_3$  was applied to remove tunnel cations ( $\text{K}^+$ ) as previously reported<sup>39</sup>. Then the nanowires were washed by DI water several times until the pH value of the solution was  $\sim 7$ .

**Materials characterizations.** In situ high-energy XRD was carried out at the 11-ID-C beamline of the Advanced Photon Source (Argonne National Laboratory). A high-energy X-ray (beam size 0.2 mm  $\times$  0.2 mm, wavelength 0.1173 Å) was used. Patterns were collected using a Perkin–Elmer area detector (placed at 1,800 mm from the samples) in the Laue diffraction geometry. The low absorption and high penetration of high-energy XRD is capable of detecting tiny phase changes that are usually invisible using lab XRD. A 3 mm hole was made in the 2032 coin cells, allowing X-rays to pass through with diffraction patterns collected once every 10 min. The holes of the coin cells were sealed by Kapton tape to prevent against air exposure.

**Microscopic analysis.** The cross-sectioned  $\text{MnO}_2$  sample for down-tunnel imaging was prepared via ultramicrotome with a diamond knife and a cutting step size of 200 nm. The embedding of the nanowires was done using epoxy resin and hardener. The TEM/STEM data were obtained using an aberration-corrected JEOL ARM 200CF microscope with a 200 kV gun and a 22 mrad convergence angle.

**EDS data** were acquired using an Oxford X-Max 100TLE windowless silicon drift detector. EELS data were obtained using a Gatan GIF Continuum (5 mm entrance aperture, dual-EELS mode,  $\sim 53$  mrad collection angle). The energy dispersion was set to be 0.2 eV per channel. A  $\sim 0.8$  eV full-width at half maximum of zero loss peak was measured to be considered as the energy resolution (Supplementary Fig. 4a), which can be considered as a moderate energy resolution, and it should have limited effect on Mn valence quantification based on peak area integration since the same analysis method is consistently applied to all samples of interest in this work. The background was subtracted using the power-law mode by placing a  $\sim 50$  eV window right before the white line peak onset positions to define the background (Supplementary Fig. 4b). The spectra were fitted using a Gaussian function with an  $R$ -square value  $> 0.99$ . The quantification of Mn valence is carried out using two independent methods: one is the Mn  $L_3/L_2$  edge white line ratio

( $L_3/L_2$ ) method, and the other is the energy difference between Mn  $L_3$  and  $L_2$ ,  $\Delta E(L_2 - L_3)$ . See Supplementary Note 1 for more information.

**Electrochemical testing.** The  $\text{MnO}_2$  cathode for battery testing is made of 10 wt% polyvinylidene difluoride binder in  $N$ -methyl-pyrrolidione, 10 wt% super P carbon and 80 wt%  $\alpha$ - $\text{MnO}_2$ . The mixture was then cast onto stainless steel foils to make the electrode. The electrode was dried at 70 °C for 4 h, followed by thorough drying at 70 °C overnight under vacuum. Battery testing was carried out using CR2032 coin cells with zinc metal as the counter electrode, 1 M  $\text{ZnSO}_4$  aqueous solution as the electrolyte and glass microfibre as the separator. Cells were cycled between 1.8 and 1.0 V. Before the battery cycling, the cross-sectioned  $\text{MnO}_2$  sample was preloaded to a TEM grid, which was then placed adjacent to the  $\text{MnO}_2$  electrode laminate and got cycled with the electrode simultaneously until intentionally terminated for ex situ TEM analysis. GITT was tested using the following procedure. The lamination of the  $\text{MnO}_2$  electrode and battery assembly operations is the same as that for the normal battery performance testing. After two normal discharge–charge cycles (30 mA  $\text{g}^{-1}$  between 1.8 V and 1.1 V), the third discharge process was targeted for the GITT measurement. The discharge current was set at 15 mA  $\text{g}^{-1}$ , and it ran for 30 min every time with an intermittent rest period of 3 h. This procedure was repeated until the discharge voltage dropped below 1.1 V.

**ICP measurement.** ICP was done using an ICP spectrometer (iCAP 7000 Series). The sample was directly obtained by collecting the electrolytes of cycled Zn– $\text{MnO}_2$  coin cells after they were opened in atmosphere.

**Computational methods.** Computational methods based on DFT are well established for examining properties of battery electrode materials<sup>40–43</sup>. All calculations here were performed using periodic DFT as implemented in the Vienna ab initio simulation package<sup>44–46</sup>. A plane-wave basis set to represent the wave functions and the projected augmented wave method were used<sup>47,48</sup>. The exchange–correlation energy was calculated within the generalized gradient approximation using the Perdew–Burke–Ernzerhof functional<sup>49</sup>. A plane-wave cut-off of 520 eV and a minimum of  $6 \times 6 \times 20$  k-points were used for each calculation. As in previous work<sup>38</sup>, the calculations were performed in a ferromagnetic spin polarized configuration and using the DFT +  $U$  approach<sup>50</sup> to account for on-site Coulomb interactions. A  $U$ – $J$  value of 5.2 eV and a  $J$  value of 1.0 eV were used for Mn, as determined in previous work<sup>38</sup>. The ionic and electronic self-consistent convergence was set to  $5 \times 10^{-2}$  and  $1 \times 10^{-5}$  eV, respectively. We performed total energy calculations in a  $1 \times 1 \times 1$  cell (24 atoms) of  $\alpha$ - $\text{MnO}_2$  using the experimental structure<sup>51</sup> at room temperature. The  $\alpha$ - $\text{MnO}_2$  crystal occurs in the tetragonal space group  $I4/m$  (no. 87) with lattice parameters  $a = b = 9.815$  Å and  $c = 2.847$  Å. In Supplementary Table 4, we show the calculated lattice parameters for  $\alpha$ - $\text{MnO}_2$ , which agree with the experimental parameters to within 3.2%. Ewald energies were used to screen for candidate low-energy configurations of  $\text{Zn}_x\text{MnO}_2$ , where  $x = 0.5$  and 0.75, due to the huge number of possible configurations. These low-energy candidates were then treated with ab initio DFT, which more fully describes the electronic effects of the system. Well-established methodology has been used in previous computational studies of battery materials to calculate ion insertion (intercalation) energies<sup>38,52</sup>. Likewise, insertion energies for H and Zn into  $\text{MnO}_2$  were calculated by comparing the energy of empty  $\text{MnO}_2$  and an  $\text{H}_2$  molecule or Zn metal with the atom intercalated within  $\text{MnO}_2$  using the most favourable ion sites. As well as ferromagnetic ordering, we performed test proton insertion calculations on  $\text{H}_{0.125}\text{MnO}_2$  with antiferromagnetic ordering, which produced the same energetic trends and lowest energy ion sites. We recognize that there is significant debate in the existing literature on the magnetic ordering in  $\alpha$ - $\text{MnO}_2$ , which we detail in Supplementary Note 2. Our DFT calculations find ferromagnetic ordering only slightly more favourable than antiferromagnetic ordering. We stress that magnetic behaviour was not our focus here, and our simulations have provided valuable atomic-scale insights and energetic trends into  $\text{Zn}^{2+}$  insertion versus  $\text{H}^+$  insertion in the charge storage process.

## Data availability

All relevant data that support the findings of this study are presented in the manuscript and Supplementary Information. Source data are available from the corresponding author upon reasonable request.

Received: 9 August 2021; Accepted: 24 May 2022;

## References

- Pan, H. et al. Reversible aqueous zinc/manganese oxide energy storage from conversion reactions. *Nat. Energy* **1**, 16039 (2016).
- Sun, W. et al. Zn/ $\text{MnO}_2$  battery chemistry with  $\text{H}^+$  and  $\text{Zn}^{2+}$  coinsertion. *J. Am. Chem. Soc.* **139**, 9775–9778 (2017).
- Blanc, L. E., Kundu, D. & Nazar, L. F. Scientific challenges for the implementation of Zn-ion batteries. *Joule* **4**, 771–799 (2020).

- 460 4. Bauer, C. et al. Charging sustainable batteries. *Nat. Sustain.* **5**, 176–178 (2022).
- 461 5. Wang, X. et al. Advances and perspectives of cathode storage chemistry in
- 462 aqueous zinc-ion batteries. *ACS Nano* **15**, 9244–9272 (2021).
- 463 6. Wu, D. et al. Quantitative temporally and spatially resolved X-ray
- 464 fluorescence microprobe characterization of the manganese dissolution–
- 465 deposition mechanism in aqueous Zn/ $\alpha$ -MnO<sub>2</sub> batteries. *Energy Environ. Sci.*
- 466 **13**, 4322–4333 (2020).
- 467 7. Chao, D. et al. An electrolytic Zn–MnO<sub>2</sub> battery for high-voltage and scalable
- 468 energy storage. *Angew. Chem. Int. Ed.* **58**, 7823–7828 (2019).
- 469 8. Mateos, M., Makivic, N., Kim, Y. S., Limoges, B. & Balland, V. Accessing the
- 470 two-electron charge storage capacity of MnO<sub>2</sub> in mild aqueous electrolytes.
- 471 *Adv. Energy Mater.* **10**, 2000332 (2020).
- 472 9. Zhao, Q. et al. Proton insertion promoted a polyfurfural/MnO<sub>2</sub>
- 473 nanocomposite cathode for a rechargeable aqueous Zn–MnO<sub>2</sub> battery.
- 474 *ACS Appl. Mater. Interfaces* **12**, 36072–36081 (2020).
- 475 10. Mathew, V. et al. Manganese and vanadium oxide cathodes for aqueous
- 476 rechargeable zinc-ion batteries: a focused view on performance, mechanism,
- 477 and developments. *ACS Energy Lett.* **5**, 2376–2400 (2020).
- 478 11. Jiao, Y. et al. Enabling stable MnO<sub>2</sub> matrix for aqueous zinc-ion battery
- 479 cathodes. *J. Mater. Chem. A* **8**, 22075–22082 (2020).
- 480 12. Zhu, X. et al. Superior-performance aqueous zinc-ion batteries based on
- 481 the in situ growth of MnO<sub>2</sub> nanosheets on V<sub>2</sub>CTX MXene. *ACS Nano* **15**,
- 482 2971–2983 (2021).
- 483 13. Yuan, Y. et al. Ordering heterogeneity of [MnO<sub>6</sub>] octahedra in tunnel-
- 484 structured MnO<sub>2</sub> and its influence on ion storage. *Joule* **3**, 471–484 (2019).
- 485 14. Yuan, Y. et al. Dynamic study of (de) sodiation in alpha-MnO<sub>2</sub> nanowires.
- 486 *Nano Energy* **19**, 382–390 (2016).
- 487 15. Yuan, Y. et al. Revealing the atomic structures of exposed lateral surfaces for
- 488 polymorphic manganese dioxide nanowires. *Small Struct.* **2**, 2000091 (2021).
- 489 16. Lindberg, S. et al. Charge storage mechanism of  $\alpha$ -MnO<sub>2</sub> in protic and
- 490 aprotic ionic liquid electrolytes. *J. Power Sources* **460**, 228111 (2020).
- 491 17. Alfaruqi, M. H. et al. Enhanced reversible divalent zinc storage in a
- 492 structurally stable  $\alpha$ -MnO<sub>2</sub> nanorod electrode. *J. Power Sources* **288**, 320–327
- 493 (2015).
- 494 18. Alfaruqi, M. H. et al. A high surface area tunnel-type  $\alpha$ -MnO<sub>2</sub> nanorod
- 495 cathode by a simple solvent-free synthesis for rechargeable aqueous zinc-ion
- 496 batteries. *Chem. Phys. Lett.* **650**, 64–68 (2016).
- 497 19. Xu, D. et al. Preparation and characterization of MnO<sub>2</sub>/acid-treated CNT
- 498 nanocomposites for energy storage with zinc ions. *Electrochim. Acta* **133**,
- 499 254–261 (2014).
- 500 20. Wu, B. et al. Graphene scroll-coated  $\alpha$ -MnO<sub>2</sub> nanowires as high-performance
- 501 cathode materials for aqueous Zn-ion battery. *Small* **14**, 1703850 (2018).
- 502 21. Lee, B. et al. Elucidating the intercalation mechanism of zinc ions into
- 503  $\alpha$ -MnO<sub>2</sub> for rechargeable zinc batteries. *Chem. Commun.* **51**, 9265–9268
- 504 (2015).
- 505 22. Zhang, N. et al. Rechargeable aqueous zinc–manganese dioxide batteries with
- 506 high energy and power densities. *Nat. Commun.* **8**, 405 (2017).
- 507 23. Lee, B. et al. Electrochemically-induced reversible transition from the
- 508 tunneled to layered polymorphs of manganese dioxide. *Sci. Rep.* **4**, 6066
- 509 (2014).
- 510 24. Yang, J. et al. Unravelling the mechanism of rechargeable aqueous Zn–MnO<sub>2</sub>
- 511 batteries: implementation of charging process by electrodeposition of MnO<sub>2</sub>.  
DOI *ChemSusChem* **13**, 4103 (2020).
- 512 25. Wang, J. et al. Superfine MnO<sub>2</sub> nanowires with rich defects toward boosted
- 513 zinc ion storage performance. *ACS Appl. Mater. Interfaces* **12**, 34949–34958
- 514 (2020).
- 515 26. Li, Y. et al. Reaction mechanisms for long-life rechargeable Zn/MnO<sub>2</sub>
- 516 batteries. *Chem. Mater.* **31**, 2036–2047 (2019).
- 517 27. Gao, X. et al. H<sup>+</sup>-insertion boosted  $\alpha$ -MnO<sub>2</sub> for an aqueous Zn-ion battery.
- 518 *Small* **16**, 1905842 (2020).
- 519 28. Huang, Y. et al. Novel insights into energy storage mechanism of aqueous
- 520 rechargeable Zn/MnO<sub>2</sub> batteries with participation of Mn<sup>2+</sup>. *Nanomicro Lett.*
- 521 **11**, 49 (2019).
- 522 29. Yuan, Y. et al. Deciphering the atomic patterns leading to MnO<sub>2</sub>
- 523 polymorphism. *Chem* **5**, 1793–1805 (2019).
- 524 30. Yuan, Y. et al. Asynchronous crystal cell expansion during lithiation of
- 525 K<sup>+</sup>-stabilized  $\alpha$ -MnO<sub>2</sub>. *Nano Lett.* **15**, 2998–3007 (2015).
31. Tan, H., Verbeeck, J., Abakumov, A. & Van Tendeloo, G. Oxidation state and
- chemical shift investigation in transition metal oxides by EELS. *Ultramicroscopy*
- 116**, 24–33 (2012).
32. Ishikawa, R. et al. Direct imaging of hydrogen-atom columns in a crystal
- by annular bright-field electron microscopy. *Nat. Mater.* **10**, 278–281
- (2011).
33. de Graaf, S., Momand, J., Mitterbauer, C., Lazar, S. & Kooi, B. J. Resolving
- hydrogen atoms at metal–metal hydride interfaces. *Sci. Adv.* **6**, eaay4312
- (2020).
34. Tompsett, D. A., Parker, S. C. & Islam, M. S. Rutile ( $\beta$ -) MnO<sub>2</sub> surfaces and
- vacancy formation for high electrochemical and catalytic performance.
- J. Am. Chem. Soc.* **136**, 1418–1426 (2014).
35. Tompsett, D. A., Parker, S. C., Bruce, P. G. & Islam, M. S. Nanostructuring of
- $\beta$ -MnO<sub>2</sub>: the important role of surface to bulk ion migration. *Chem. Mater.*
- 25**, 536–541 (2013).
36. Vasiliev, I., Magar, B. A., Duay, J., Lambert, T. N. & Chalamala, B. Ab initio
- studies of hydrogen ion insertion into  $\beta$ -, R-, and  $\gamma$ -MnO<sub>2</sub> polymorphs
- and the implications for shallow-cycled rechargeable Zn/MnO<sub>2</sub> batteries.
- J. Electrochem. Soc.* **165**, A3517 (2018).
37. Balachandran, D., Morgan, D. & Ceder, G. First principles study of
- H-insertion in MnO<sub>2</sub>. *J. Solid State Chem.* **166**, 91–103 (2002).
38. Tompsett, D. A. & Islam, M. S. Electrochemistry of hollandite  $\alpha$ -MnO<sub>2</sub>:
- Li-ion and Na-ion insertion and Li<sub>2</sub>O incorporation. *Chem. Mater.* **25**,
- 2515–2526 (2013).
39. Yuan, Y. et al. The influence of large cations on the electrochemical properties
- of tunnel-structured metal oxides. *Nat. Commun.* **7**, 13374 (2016).
40. Sharpe, R. et al. Redox chemistry and the role of trapped molecular O<sub>2</sub> in
- Li-rich disordered rocksalt oxyfluoride cathodes. *J. Am. Chem. Soc.* **142**,
- 21799–21809 (2020).
41. Naylor, A. J. et al. Depth-dependent oxygen redox activity in lithium-rich
- layered oxide cathodes. *J. Mater. Chem. A* **7**, 25355–25368 (2019).
42. Li, Y. et al. Fluid-enhanced surface diffusion controls intraparticle phase
- transformations. *Nat. Mater.* **17**, 915–922 (2018).
43. Tapia-Ruiz, N. et al. High voltage structural evolution and enhanced Na-ion
- diffusion in P2-Na<sub>2/3</sub>Ni<sub>1/3-x</sub>Mg<sub>x</sub>Mn<sub>2/3</sub>O<sub>2</sub> (0 ≤ x ≤ 0.2) cathodes from diffraction,
- electrochemical and ab initio studies. *Energy Environ. Sci.* **11**, 1470–1479
- (2018).
44. Kresse, G. & Furthmüller, J. Efficient iterative schemes for ab initio total-
- energy calculations using a plane-wave basis set. *Phys. Rev. B* **54**, 11169
- (1996).
45. Kresse, G. & Hafner, J. Ab initio molecular dynamics for liquid metals.
- Phys. Rev. B* **47**, 558–561 (1993).
46. Kresse, G. & Hafner, J. Ab initio molecular-dynamics simulation of the liquid-
- metal–amorphous-semiconductor transition in germanium. *Phys. Rev. B* **49**,
- 14251 (1994).
47. Blöchl, P. E. Projector augmented-wave method. *Phys. Rev. B* **50**, 17953
- (1994).
48. Kresse, G. & Joubert, D. From ultrasoft pseudopotentials to the projector
- augmented-wave method. *Phys. Rev. B* **59**, 1758 (1999).
49. Perdew, J. P., Burke, K. & Ernzerhof, M. Generalized gradient approximation
- made simple. *Phys. Rev. Lett.* **77**, 3865 (1996).
50. Dudarev, S., Botton, G., Savrasov, S., Humphreys, C. & Sutton, A.
- Electron-energy-loss spectra and the structural stability of nickel oxide: an
- LSDA+U study. *Phys. Rev. B* **57**, 1505 (1998).
51. Kondrashev, Y. D. & Zaslavskii, A. The structure of the modifications
- of manganese (IV) oxide. *Izv. Akad. Nauk SSSR Ser. Fiz.* **15**, 179–186
- (1951).
52. Islam, M. S. & Fisher, C. A. J. Lithium and sodium battery cathode materials:
- computational insights into voltage, diffusion and nanostructural properties.
- Chem. Soc. Rev.* **43**, 185–204 (2014).

## Acknowledgements

This work was financially supported by the Natural Science Foundation of China (grant no. 52002287). R.S.-Y. is thankful to National Science Foundation (NSF) Award CBET-1805938. R.S. and M.S.I. thank the EPSRC (LiBatt programme grant EP/M0009521/1) and the Faraday Institution (CATMAT project FIRG016, FIRG035) for financial support, and the HEC Materials Chemistry Consortium (EP/R029431), the Isambard HPC (EP/P020224/1) and the Balena HPC service (Bath) for supercomputer facilities. R.S. and M.S.I. gratefully acknowledge useful discussions with P. Zarabadi-Poor (Oxford), L. Morgan (Bath), K. McColl (Bath), M. J. Clarke (Bath) and J. Dawson (Newcastle). Work at Argonne National Laboratory was supported by the US Department of Energy (DOE), Office of Energy Efficiency and Renewable Energy, Vehicle Technologies Office. Argonne National Laboratory is operated for DOE Office of Science by UChicago Argonne, LLC, under contract number DE-AC02-06CH11357. Use of the Advanced Photon Source (APS) {Beamline 9-BM} at Argonne National Laboratory, Office of Science user facility, was supported by the US Department of Energy, Office of Science, Office of Basic Energy Sciences, under contract no. DE-AC02-06CH11357. This work made use of instruments in the Electron Microscopy Service (Research Resources Center, UIUC). We acknowledge Quantitative Bio-element Imaging Center (QBIC) at Northwestern University (US) for assistance of ICP measurement. We acknowledge Thermo Fisher Scientific's Shanghai Nanoport, particularly S. Liu, for their consultative help in atomic imaging of light atoms using electron microscopy.

## Author contributions

Y.Y. initiated the experimental design and wrote the manuscript with R.S., M.S.I., K.H., R.S.-Y. and J.L. Y.Y., K.H., M.T.S. and M.C. carried out microscopic experiments and data analyses. Y.Y., C.L., T.L., W.Y. and K.A. carried out electrochemical experiments and data analyses. H.J. and S.W. contributed to discussions and offered guidance to the electrochemical data analysis. R.S. and M.S.I. designed, carried out and analysed the

526 DFT calculations. Y.Y. and T.L. carried out synchrotron X-ray experiments. All authors  
527 contributed to the results discussion and writing of the manuscript.

528  
529 **Competing interests**

530 The authors declare no competing interests.

531  
532 **Additional information**

533 **Supplementary information** The online version contains supplementary material  
534 available at <https://doi.org/10.1038/s41893-022-00919-3>.

535  
536  
537  
538

**Correspondence and requests for materials** should be addressed to Kun He, Reza Shahbazian-Yassar, M. Saiful Islam or Jun Lu.

**Peer review information** *Nature Sustainability* thanks Dipan Kundu and the other, anonymous, reviewer(s) for their contribution to the peer review of this work.

**Reprints and permissions information** is available at [www.nature.com/reprints](http://www.nature.com/reprints).

**Publisher's note** Springer Nature remains neutral with regard to jurisdictional claims in published maps and institutional affiliations.

© This is a U.S. Government work and not under copyright protection in the US; foreign copyright protection may apply 2022

Uncorrected proofs

# QUERY FORM

<b>Nature Sustainability</b>	
<b>Manuscript ID</b>	[Art. Id: 919]
<b>Author</b>	Yifei Yuan

**AUTHOR:**

The following queries have arisen during the editing of your manuscript. Please answer by making the requisite corrections directly in the e-proofing tool rather than marking them up on the PDF. This will ensure that your corrections are incorporated accurately and that your paper is published as quickly as possible.

<b>Query No.</b>	<b>Nature of Query</b>
Q1:	Please check your article carefully, coordinate with any co-authors and enter all final edits clearly in the eproof, remembering to save frequently. Once corrections are submitted, we cannot routinely make further changes to the article.
Q2:	Note that the eproof should be amended in only one browser window at any one time; otherwise changes will be overwritten.
Q3:	Author surnames have been highlighted. Please check these carefully and adjust if the first name or surname is marked up incorrectly. Note that changes here will affect indexing of your article in public repositories such as PubMed. Also, carefully check the spelling and numbering of all author names and affiliations, and the corresponding email address(es).
Q4:	You cannot alter accepted Supplementary Information files except for critical changes to scientific content. If you do resupply any files, please also provide a brief (but complete) list of changes. If these are not considered scientific changes, any altered Supplementary files will not be used, only the originally accepted version will be published.
Q5:	If applicable, please ensure that any accession codes and datasets whose DOIs or other identifiers are mentioned in the paper are scheduled for public release as soon as possible, we recommend within a few days of submitting your proof, and update the database record with publication details from this article once available.
Q6:	In the sentence beginning 'Before cation removal ...', please confirm the insertion of 'energy-dispersive X-ray spectroscopy' as the definition of 'EDS' is correct.
Q7:	On Fig. 1, please confirm all labels are correct as edited.
Q8:	In the sentence beginning 'To further study the phase evolution ...', please confirm the insertion of 'X-ray diffraction' as the definition of 'XRD' is correct.
Q9:	Please confirm that edits to the sentence beginning 'New peaks immediately appear ...' have retained the intended meaning.
Q10:	Please note, we reserve 'significant' and its derivatives for statistical significance. Please reword where this is not the intended meaning (for example to important, notable, substantial); there are 3 instances throughout your text.
Q11:	Please explain the inset in Fig. 2e.
Q12:	We conform to the style that vectors are set in bold roman font. The magnitude of a vector is set in nonbold italics, as are scalar components, tensors and matrices. Please ensure your text is consistent with this throughout.

